

Theoretical Investigation of electronic and optical properties of 2-Dimensional Janus Material WSeTe under compression

SHIKHARKYA DEB^{a,1}^aM.Sc (II year student) Harish Chandra Research Institute

Abstract—The electronic and optical properties of WSeTe monolayer have been optimized under a varying range of pressure extending from 0.763 GPa upto 2.446 GPa using simulations based on Density Functional Theory. At all pressures, the material is semi-conductive and the band gap reduces. The optical function analysis reveals an increase of conductivity and absorption near the violet region making it extremely useful in solar cells. Optical properties meet an enhancement under an application of uniaxial pressure. Inferences suggest for the applications of WSeTe in optical devices for its photovoltaic properties.

Keywords—DFT(Density Functional Theory), Phonon Dispersion, Optical Properties, Monolayer

1. Introduction

A range of two-dimensional materials due to their unique and excellent electronic, optical, and mechanical properties can replace the silicon-based semiconductors. The silicon-based semiconductors are facing replacement with increase developments, which also proves Moore's law

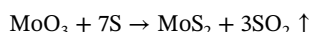
$$N(t) = N_0 \times 2^{t/\tau}$$

where:

- $N(t)$ = Transistor count at time t ,
- N_0 = Initial count,
- τ = Doubling period (2 years).

The most striking among the new 2D materials are the transition metal dichalcogenides (TMDs) with the molecular formula of MX_2 , are among the most appealing because of their unique physical properties, such as the giant spin splitting induced by strong spin-orbit coupling (SOC) from the transition metal atoms at the top of the valence band, and the degenerate but unequal energy valley caused by the inversion symmetry breaking. The electronic and optical properties of materials largely depend on their crystal structure. Different from the traditional 2D materials the properties of MX_2 is of great interest in electronics, spintronics and optoelectronics. Nanomaterials have attracted extensive attention and research. The most striking nano structures 2D Janus materials, formed of asymmetric heterogeneous structure have been of wide attention. Janus nano materials with their surfaces composed of metal atoms have excellent electronic and optical properties, which reinforce the fact that the properties of Janus nanostructures largely depend on the type of structure. TMD such as MX_2 ($M=W/Mo$, $X/Y=Se,S,Te$), have been synthesized by vulcanization or selenidation experiments by CVD (Chemical Vapour Deposition) **Vulcanization (Sulfurization) by CVD Process**:

- **Precursor Deposition:** A thin film of metal (Mo, W) or oxide (MoO_3, WO_3) is deposited on a substrate (SiO_2/Si , sapphire).
- **Sulfur Vapor Introduction:** Solid Sulfur (S) is heated ($100-200^\circ C$)
- **Reaction:**
Vulcanization of MoO_3 :



- **Outcome:** Forms atomically thin MoS_2 or WS_2 layers (1-3 layers)

Selenidation by CVD Process:

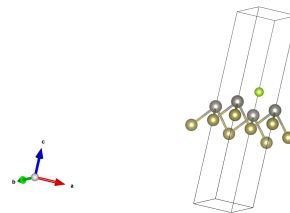
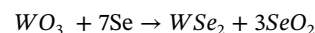
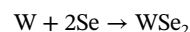


Figure 1. Monolayer of WSeTe (2-Dimensional)

- **Precursor Preparation:** Similar to vulcanization but uses Se powder (heated to $250-350^\circ C$ for caporization).
- **High-Temperature Reaction ($700-900^\circ C$):**



- **Outcome:** Produces $MoSe_2$ or WSe_2 with tunable bandgaps ($1.5 eV$ for $MoSe_2$)

Different from the mirror symmetrical structures of MoS_2 and $MoSe_2$, the $MoSe$ monolayer is formed by selective selenization of the top atomic layer in a single layer MoS_2 . The electronegativity difference between sulfur atom and selenium atom causes the interlayer polarization of Janus material to couple with the interlayer built-in an inherent polarization field which provides an additional degree of freedom to modulate its physiochemical properties and gains an attention because of its novel features and potential applications. 2D Janus WSeTe monolayer has caught the attention based on first principles calculations, researches have taken interest in studying the thermoelectric transport characteristics of Janus WSeTe, and also studied the electronic properties of WSeTe heterostructures. In this context, the report consists of an extensive study of the electronic and photodiode characteristics. Both experimentally and theoretically Janus transition metal dichalcogenides have become a source keen interest for research due to its mirror asymmetry, such as strong Rashba effects and out-of-plane voltage electric polarization, providing broad spectrum of applications involving sensors, brakes and other electromechanical devices. The report analyzes that under strain the WSeTe monolayer, a typical two-dimensional material shows very good physical and chemical properties. Under uniaxial strain WSeTe monolayer prevails in the domain of semiconductor. On this basis the study of WSeTe monolayer begins in this report.

The system is subjected to uniaxial strain and externally applied electric field to adjust the band alignment of WSeTe monolayer to promote its great scientific application, and its electronic high switching and optical properties are studied. The calculated results here can provide some potential reference information for practical application of WSeTe monolayer in the near future.

2. Computational Methodology

2.1. Density Functional Theory

The Schrodinger or Dirac equation describes the motion of atoms and molecules. The computational complexity to obtain the exact solution grows exponentially with the number of electrons N . Calculating exact ground-state wave function is prohibitively expensive when N is more than a few dozen. Therefore, it has been a challenge to

develop a powerful and accurate electronic structures. The numerical approaches include two methods, one being the many-body wave function itself and attempts to find good approximations to the exact wavefunction. The other is the density functional theory (DFT). By using the electron density $\rho(r)$ (a function of three coordinate variables) as the fundamental variable instead of the many-body wave function (a function of 3N coordinate variables), DFT has drastically reduced the computational cost. Therefore, DFT is the most widely used method for electronic structure calculations of solids.

Components of the Total Electronic Energy :-

$$E_{tot} = E_T + E_V + E_J + E_X + E_C$$

E_{tot} refers to the total electronic energy, E_T as the total kinetic energy, E_V is the total potential energy of the electrons due to the average Coulomb repulsion between pairs of electrons, E_X is the total quantum mechanical exchange energy of the electrons, and E_C is the total correlation energy of the electrons.

Modern DFT has its roots in the work of Walter Kohn, Lu Jeu Sham, and Pierre Hohenberg. Hohenberg and Kohn showed that a universal functional for the total electronic energy of an atom, molecule, or ion, $E_{tot}[n(r)]$, can be defined in terms of the electron density $n(r)$, and also showing that the total electronic energy and other observable properties are a functional of $n(r)$. The electron density can be represented using different types of mathematical functions. The DFT calculations were performed using planewave functions as a basis sets. The infinite extents of these made them favourable for computations on extended structures such as metal surfaces or crystalline solids. For calculations of discrete atoms and molecules, atom-centered basis sets are generally more appropriate. The electron density is represented by a single atom-centered Gaussian basis function, $\chi_i(r)$. In general, the optimization of the total electron density, $n(r)$, is accomplished by systematic variation of the linear expansion coefficients, c_i in the equation below to obtain the lowest possible energy

$$n(r) = (\sum_{i=1}^N (c_i \chi_i(r))^2)$$

2.2. Schrodinger Equation

Density Functional theory is an approach to studying the Schrodinger equation by writing quantities of interest, such as energies, in terms of the particle density, instead of in terms of the wave function. This can simplify computations considerably, especially when the number of particles is large.

To be more specific, consider an N-electron system, with Hamiltonina given by

$$H = T + V_{cc} + V$$

where,

$$T = -\frac{1}{2} \sum_{j=1}^N \nabla_j^2,$$

$$V_{cc} = \sum_{1 \leq i \leq N} \frac{1}{|\vec{r}_i - \vec{r}_j|},$$

$$V = \sum_{i=1}^N v(\vec{r}_i) = \sum_{i=1}^N \int d^3r \delta(\vec{r} - \vec{r}_i) v(\vec{r})$$

and where v is the potential coming from the external forces on the electrons. Here T is the kinetic energy term, V_{cc} is the repulsive term Coulomb potential energy between the electrons, and V is the potential energy due to external forces. We are using atomic units: this means Planck's constant \hbar , the electron mass m_e , and the magnitude of the electron charge e are all equal to 1. The unit of distance is the Bohr radius $a_0 = \hbar^2/(me^2)$, and the unit of energy is the hartree $\epsilon_0 = e^2/a_0$. One Bohr radius is about 5.29×10^{-11} meters and one hartree is about 27.2 eV. We are ignoring the sizes of nuclei, the movements of the nuclei, spin and the relativistic effects.

For example, consider a system of N electrons in a molecule made up of M atoms. Then v is the attractive Coulomb potential energy arising from the M atomic nuclei, given by

$$v(\vec{r}) = \sum_{k=1}^M \frac{-Z_k}{|\vec{r} - \vec{R}_k|},$$

where \vec{R}_k is the position of the kth nucleus and Z_k is the number of protons it has.

The density is defined by

$$n(\vec{r}) = \langle \psi | n(\vec{r}) | \psi \rangle = \int d^3r_1 \int d^3r_2 \dots \int d^3r_N \psi^*(\vec{r}_1, \dots, \vec{r}_N) \sum_{i=1}^N \delta(\vec{r} - \vec{r}_i) \psi(\vec{r}_1, \dots, \vec{r}_N).$$

Note that $\int d^3r n(\vec{r}) = N$, and for any region U , the quantity $\int_U d^3r n(\vec{r})$, gives the expected value of the number of electrons to be found in U .

The entire point about Density Functional Theory is to compute in terms of n rather than computing in terms of ψ . The basic result is the Hohenberg-Kohn Theorem, which portrays the fact that is $n(r)$ is a ground state density, then no information is lost by doing this.

2.3. Single Body Problem

The essence of the single-body problem in DFT arises from the Hohenberg-Kohn (HK) theorems, which fundamentally shift the focus from the intractable many-body wavefunction to the much simpler electron density. The first HK theorem states that the external potential $v(r)$ of a many-electron system is uniquely determined, up to an additive constant, by its ground-state electron density $n(r)$. This implies that all ground-state properties, including the total energy, are unique functionals of $n(r)$. The second HK theorem then introduces a variational principle, stating that for any trial density \tilde{n} , the energy functional $E_v[\tilde{n}]$ will yield an energy greater than or equal to the true ground-state energy E_0 , with equality holding for the true ground-state density $n_0(r)$. While these theorems prove the existence of such a functional, they do not provide its explicit form. This is where the Kohn-Sham (KS) scheme enters, transforming the problem into a solvable "single-body" or "auxiliary non-interacting" system. The KS derivation introduces a fictitious system of non-interacting electrons moving in an effective local potential $v_{eff}(r)$, such that their ground-state density $n_0(r)$ is identical to that of the real interacting system. The total energy functional is then written as $E[n] = T_s[n] + \int v(r)n(r)dr + E_H[n] + E_{xc}[n]$, where $T_s[n]$ is the kinetic energy of the non-interacting system, $E_H[n]$ is the classical Hartree (Coulomb) energy, and $E_{xc}[n]$ is the unknown exchange-correlation energy functional, defined to encapsulate all the complex many-body effects (true kinetic energy correlation, exchange, and correlation contributions to potential energy). Minimizing this functional with respect to $n(r)$ under the constraint that the density integrates to the total number of electrons N, leads to the set of effective single-particle Kohn-Sham equations:

$$[-\frac{\hbar^2}{2m} \nabla^2 + v_{eff}(r)]\phi_i(r) = \epsilon_i \phi_i(r)$$

where $v_{eff}(r) = v(r) + \int \frac{n(r')}{|\vec{r} - \vec{r}'|} dr' + v_{xc}(r)$, and $v_{xc}(r) = \frac{\delta(E_{xc})}{\delta n(r)}$ is the exchange-correlation potential. The electron density is then constructed from the sum of the squares of the occupied single-particle Kohn-Sham orbitals: $n(r) = \sum_{i=1}^N |\phi_i(r)|^2$. This elegant framework reduces the formidable many-electron problem to the self-consistent solution of a set of one-electron-like Schrödinger equations, thereby making the theory computationally tractable, albeit with the crucial approximation residing in the form of $E_{xc}[n]$.

2.4. Many-Body Problem

The most challenging and central aspect of electronic structure theory is the many-body problem. The core of this problem lies in solving the time-independent Schrodinger equation for a system of N interacting electrons and M nuclei. The Hamiltonian for such system, in atomic units, is given by:

$$H = \sum_{i=1}^N (-\frac{1}{2} \nabla_i^2) + \sum_{i=1}^M (-\frac{1}{2M_i} \nabla_i^2) + \sum_{i < j} \frac{1}{|\vec{r}_i - \vec{r}_j|} - \sum_{i=1}^N \sum_{I=1}^M \frac{Z_I}{r_{i-I}} + \sum_{I < J} \frac{Z_I Z_J}{|R_I - R_J|}$$

Here, the first term represents the kinetic energy of the electrons, the

second is the kinetic energy of the nuclei, the third is the electron-electron repulsion, the fourth is the electron-nucleus attraction, and the last is the nucleus-nucleus repulsion. The formidable difficulty arises from the electron-electron interaction term ($\sum_{i<j} \frac{1}{|r_i - r_j|}$). This term couples the motion of all electrons, meaning the behavior of one electron instantaneously depends on the positions of all others. Consequently, the many-electron wavefunction $\psi(r_1, \dots, r_N)$ is a complex function of the $3N$ spatial coordinates (plus spin), making its direct numerical solution intractable for any but the smallest systems (e.g., $N=2$ for Helium, exactly). The dimensionality of this wavefunction grows exponentially with N , leading to the so-called "exponential wall" in computational cost. For instance, if one were to discretize each electron's position with just L points, the wavefunction would require L^N values to describe it, which quickly becomes astronomical.

The challenge is further compounded by the indistinguishability of electrons and the Pauli exclusion principle, which necessitate the wavefunction to be antisymmetric with respect to the exchange of any two electrons. Traditional many-body approaches, such as Hartree-Fock, attempt to approximate the many-body wavefunction as a single Slater determinant, effectively treating electron-electron interactions in an averaged, mean-field way. However, these methods miss a crucial part of the electron correlation, which is the instantaneous avoidance of electrons. Calculating this "correlation energy" rigorously typically involves highly computationally intensive methods that scale very poorly with the number of electrons.

2.5. Thomas-Fermi theory

The theory developed independently by Thomas and Fermi for the ground state of complex atoms or ions having large number of electrons is based on statistical and semi-classical considerations. The N electrons of the system are treated as a Fermi electron gas in the ground state, confined to a region of space by a central potential $V(r)$ which vanishes at infinity. It is assumed that this potential is slowly varying over a distance which is large compared with the de-Broglie wavelength of the electrons, so that enough electrons are present in a volume where $V(r)$ is nearly constant, and the statistical approach used in studying the Fermi electron gas can be applied. In addition, since the number of electrons is large, many of them have high principle quantum numbers, so that semi-classical methods should be useful.

The aim of the Thomas-Fermi model is to provide a method of calculating the potential $V(r)$ and the electron density $\rho(r)$. These two quantities can first be related by using the following arguments. The total energy of an electron is written as $p^2/2m + V(r)$, and this energy cannot be positive, otherwise the electron would escape to infinity. Since the maximum kinetic energy of an electron in a Fermi electron gas at 0K is the Fermi energy E_F , we write for the total energy of the most energetic electrons of the system the classical equation

$$E_{max} = E_F + V(r) \quad (1)$$

It is clear that E_{max} must be independent of r , because if it were not the case electrons would migrate to the region of space where E_{max} is smallest in order to lower the total energy of the system. Furthermore, we must have $E_{max} \leq 0$. We note from the equation (1) that the quantity k_F is now a function of r . That is

$$k_F^2 = \frac{2m}{\hbar^2} [E_{max} - V(r)], \text{ for the density function we then have,}$$

$\rho(r) = \frac{1}{3\pi^2} \left(\frac{2m}{\hbar^2} \right)^{3/2} [E_{max} - V(r)]$, and we see that ρ vanishes when $V = E_{max}$. In the classically forbidden region $V > E_{max}$ we must set $\rho = 0$, since otherwise equation (1) would yield a negative value of the maximum kinetic energy E_F . Let us denote by,

$$\phi(r) = -\frac{1}{e} V(r) \quad (2)$$

the electrostatic potential and by $\phi_0 = -E_{max}/e$ a non-negative constant. Setting

$$\phi(r) = \phi(r) - \phi_0 \quad (3)$$

we see that $\rho(r)$ and $\phi(r)$ are related by

$$\rho(r) = \frac{1}{3\pi^2} \left(\frac{2m}{\hbar^2} \right)^{3/2} [e\phi(r)]^{3/2} \quad \phi \geq 0 \quad (4)$$

$$= 0 \quad \phi < 0 \quad (5)$$

Treating the charge density $-\rho(r)$ of the electrons as continuous, we may use Poisson's equation of electrostatics to write

$$\nabla^2 \phi(r) = \frac{1}{r} \frac{d^2}{dr^2} [r\phi(r)] = \frac{e}{\epsilon_0} \rho(r) \quad (6)$$

Using equation (4) and (6) are two simultaneous equations for $\rho(r)$ and $\phi(r)$. Eliminating $\rho(r)$ from these equations, we find that for $\phi \geq 0$

$$\frac{1}{r} \frac{d^2}{dr^2} [r\phi(r)] = \frac{e}{3\pi^2 \epsilon_0} \left(\frac{2m}{\hbar^2} \right)^{3/2} [e\phi(r)]^{3/2}, \quad \phi \geq 0 \quad (7)$$

On the other hand, when $\phi < 0$ we see from equation (5) and (6) that

$$\frac{d^2}{dr^2} [r\phi(r)] = 0, \quad \phi < 0 \quad (8)$$

The important equation (8) can be re written in dimensionless form as

$$r\phi(r) = \frac{Ze}{4\pi\epsilon_0} \chi(x) \quad r = bx \quad b = \frac{(3\pi)^{2/3}}{2^{7/3}} a_0 Z^{-1/3} \quad (9)$$

$$\frac{d^2}{dx^2} \chi = x^{-1/2} \chi^{3/2} \quad \chi \geq 0 \quad (10)$$

Known as the *Thomas - Fermi equation*. from equation (2), (3) and (10) and remembering that $\phi_0 = 0$ for a neutral atom, we see that in the Thomas-Fermi model the central potential $V(r)$ is given for neutral atoms by

$$V(r) = -\frac{Ze^2}{4\pi\epsilon_0 r} \chi \quad \text{for } r \rightarrow 0 \quad V(r) \approx \frac{e^2}{a\pi\epsilon_0} \left(-\frac{Z}{r} + 1.794 \frac{Z^{4/3}}{a_0} \right) \quad (11)$$

2.6. Born-Oppenheimer Approximation

The Born-Oppenheimer (BO) approximation is a cornerstone of quantum chemistry and condensed matter physics, providing a simplification that makes the notoriously complex many-body Schrödinger equation tractable for molecular and solid-state systems. The approximation stems from the immense mass difference between atomic nuclei and electrons. Nuclei are thousands of times heavier than electrons, implying they move significantly slower. **Theoretical Basis and Derivation:**

The full time-independent molecular Schrödinger equation for a system of N electrons and M nuclei is given by:

$H_{tot} \psi(r, R) = E_{tot} \psi(r, R)$ where r denotes the collective electronic coordinates (r_1, \dots, r_N) and R denotes the collective nuclear coordinates (R_1, \dots, R_N). The total Hamiltonian H_{tot} can be decomposed into:

$$H_{tot} = T_e + T_N + V_{ee} + V_{eN} + V_{NN} \quad \text{Here:}$$

- $T_e = \sum_{i=1}^N -\frac{\hbar^2}{2m_e} \nabla_i^2$ is the kinetic energy of the electrons
- $T_N = \sum_{I=1}^M -\frac{\hbar^2}{2M_I} \nabla_I^2$ is the kinetic energy operator of the nuclei
- $V_{ee} = \sum_{i<j}^N \frac{e^2}{4\pi\epsilon_0|r_i-r_j|}$ is the electron electron repulsion
- $V_{eN} = \sum_{i=1}^N \sum_{I=1}^M -\frac{Z_I e^2}{4\pi\epsilon_0|r_i-R_I|}$ is the electron nucleus attraction
- $V_{NN} = \sum_{I<J}^M \frac{Z_I Z_J e^2}{4\pi\epsilon_0|R_I-R_J|}$ is the nucleus nucleus repulsion

The BO approximation is based on the idea that due to their much larger mass, nuclei effectively appear stationary to the rapidly moving electrons. This allows for a separation of variables in the total wavefunction. , the nuclear kinetic energy term (T_N) is neglected, and the nuclear coordinates R are treated as fixed parameters. The remaining Hamiltonian is the electronic Hamiltonian, $H_{el}(r; R)$. The BO approximation simplifies the problem by decoupling the fast electronic motion from the slow nuclear motion. This allows for the calculation of molecular geometries, vibrational frequencies, and reaction pathways by exploring the potential energy surfaces $E_k(R)$.

2.7. Hartree-Fock Approximation

In the Hartree-Fock approach, it is assumed, in accordance with the independent particle approximation and the Pauli exclusion principle, that the N -electron wave function is a Slater determinant ϕ , or in other words an antisymmetric product of individual electron spin-orbitals. The optimum Slater determinant is then obtained by using the variational method to determine the 'best' individual electron spin-orbitals. The Hartree-Fock equations take the (deceptively) simple form

$$[-\frac{1}{2}\nabla^2 + V(q_i)]u_\lambda(q_i) = E_\lambda u_\lambda(q_i) \quad (12)$$

For the Hartree-Fock equation (12) it is seen that for a given state of the atom or ion, characterised by the occupied spin-orbitals, all the electrons move in the same Hartree-Fock potential. Moreover, for a given potential, two spin-orbitals u_λ and $u_{\lambda'}$, corresponding to different individual energies $E_\lambda \neq E_{\lambda'}$, are easily orthogonal. For atoms (ions) with closed subshells the Central Field Approximation is exact within the framework of the Hartree-Fock method. The Radial equation then reads as:

$$[-\frac{1}{2}\frac{d^2}{dr^2} + \frac{l(l+1)}{2r^2} - \frac{Z}{r} + V^d - V^{ex}]P_{nl}(r) = E_{nl}P_{nl}(r_i) \quad (13)$$

where,

$$V^d = \sum_{n'l'} V_{n'l'}^d \quad (14)$$

$$= \sum_{n'l'} 2(2l'+1) \int_0^\infty |P_{n'l'}(r_j)|^2 \frac{1}{r_{\geq}} dr_j \quad (15)$$

$$V^{ex}P_{nl}(r_i) = \sum_{n'l'} V_{n'l'}^{ex} P_{nl}(r_i) \quad (16)$$

$$= \sum_{n'l'} \sum_{L=|l-l'|}^{l+l'} \frac{2l'+1}{2L+1} \langle l'l'00|L0 \rangle I \quad (17)$$

$$I = [\int_0^\infty P_{n'l'}^*(r_j) \frac{r_{<}^L}{r_{>L+1}} P_{nl}(r_j) dr_j] P_{n'l'}(r_i) \quad (18)$$

where $r_{>} = \max(r_i, r_j)$, $r_{<} = \min(r_i, r_j)$, $|l-l'| \leq L \leq l+l'$

For atoms (ions) having incomplete subshells, the Hartree-Fock potential V is no longer spherically symmetric. However, this departure from spherical symmetry is often small, since in many cases (in particular for the ground state) it arises from only one incomplete subshell. An approximate Hartree-Fock central field V is then obtained by averaging V over spin directions and angles.

2.8. Hohenberg-Kohn Theorem

First Hohenberg-Kohn Theorem

The first theorem states that: **the external potential $V_{\text{ext}}(\mathbf{r})$ is a unique functional of the ground-state electron density $\rho_0(\mathbf{r})$; since, in turn, $V_{\text{ext}}(\mathbf{r})$ fixes the Hamiltonian \hat{H} , the full many-particle ground state is a unique functional of $\rho_0(\mathbf{r})$.**

Since the complete ground-state energy is a functional of the ground-state electron density, so must be its individual components. We can write this (reverting to the subscript 'Ne' to specify the kind of external potential present in our case, which is fully defined by the attraction due to the nuclei):

$$E_0[\rho_0] = T[\rho_0] + E_{ee}[\rho_0] + E_{Ne}[\rho_0] \quad (19)$$

$$E_0[\rho_0] = \int \rho_0(\mathbf{r}) V_{Ne}(\mathbf{r}) d\mathbf{r} + T[\rho_0] + E_{ee}[\rho_0] \quad (20)$$

Collecting the system-independent parts into a new quantity, the **Hohenberg-Kohn functional $F_{HK}[\rho_0]$** , we arrive at:

$$E_0[\rho_0] = \int \rho_0(\mathbf{r}) V_{Ne}(\mathbf{r}) d\mathbf{r} + F_{HK}[\rho_0] \quad (21)$$

The ground-state density uniquely determines the Hamiltonian operator, which characterizes all states of the system, both ground and excited. Thus, all properties of all states are formally determined by the ground-state density (even though we would need functionals other than $\int \rho(\mathbf{r}) V_{Ne}(\mathbf{r}) d\mathbf{r} + F_{HK}[\rho]$, which is the functional constructed to deliver E_0 but not properties of electronically excited states). In the next section, we will see that the reason why Density Functional Theory is usually termed a ground-state-only theory is a consequence of the Second Hohenberg-Kohn Theorem. On the other hand, it is only the ground-state density that contains the information about positions and charges of the nuclei, allowing the mapping from density to external potential; the density of an excited state cannot be used for this purpose.

Second Hohenberg-Kohn Theorem: Variational Principle

This theorem states that the $F_{HK}[\rho]$, the functional that delivers the ground state energy density ρ_0 . This is of course nothing else than our old friend, the variational principle which in the present context can be expressed as

$E_0 \leq E[\tilde{\rho}] + E_{Ne}[\tilde{\rho}] + E_{ee}[\tilde{\rho}]$. The trial density $\tilde{\rho}(r)$ defines its own Hamiltonian H and hence its own wave function $\tilde{\psi}$. This wave function can now be taken as the trial wave function for the Hamiltonian generated from the true external potential V_{ext} . Thus, we arrive at

$$\langle \tilde{\psi} | H | \tilde{\psi} \rangle = T[\tilde{\rho}] + V_{ee}[\tilde{\rho}] + \int \tilde{\rho}(\vec{r}) V_{\text{ext}} d\vec{r} = E[\tilde{\rho}] \geq E_0[\rho_0] = \langle \psi_0 | H | \psi_0 \rangle \quad (22)$$

which is the desired result.

2.9. Kohn-Sham equations

2.9.1. The Kohn-Sham trick

In pure DFT the energy is given by the functional:

$$E[n] = E_{\text{kin}}[n] + E_{\text{coul}}[n] + E_{\text{xc}}[n] + E_{\text{ext}}[n] \quad (23)$$

and the biggest obstacle is the lack of an accurate expressions for the kinetic energy functional. With Kohn-Sham DFT approach we can rewrite the energy as

$$E[n] = E_{\text{kin,KS}}[n] + (E_{\text{kin}}[n] - E_{\text{kin,KS}}[n]) + E_{\text{coul}}[n] + E_{\text{xc}}[n] + E_{\text{ext}}[n] \quad (24)$$

Where $E_{\text{kin,KS}}[n]$ is the energy of the non interacting kohn sham electrons. We have an exact expression for $E_{\text{kin,KS}}[n]$, albeit in terms of molecular orbitals, rather than the density. The difference ($E_{\text{kin}}[n] -$

$E_{kin,KS}[n]$ is smaller than the errors in the approximations for $E_{kin}[n]$ in pure orbital free DFT.

2.9.2. Kohn-sham energy expression

The total energy functional is now written as the sum of a functional of the molecular orbitals for the kinetic energy part and functionals of the density for the rest of the energy components

$$\begin{aligned}
 I &= (E_{kin}[n] - E_{kin,KS}[n]) + E_{xc}[n] \quad (25) \\
 E[n] &= E_{kin,KS}[n] + E_{Coul}[n] + E_{ext}[n] + (E_{kin}[n] - E_{kin,KS}[n]) + E_{xc}[n] \\
 &= 2 \sum_{i=1}^{N_{el}/2} \int \psi_i^*(\mathbf{r}) \left(-\frac{1}{2} \nabla^2 \right) \psi_i(\mathbf{r}) d\mathbf{r} + E_{Coul}[n] + E_{ext}[n] + I \\
 &= 2 \sum_{i=1}^{N_{el}/2} \int \psi_i^*(\mathbf{r}) \left(-\frac{1}{2} \nabla^2 \right) \psi_i(\mathbf{r}) d\mathbf{r} + E_{Coul}[n] + E_{ext}[n] + I \\
 &= 2 \sum_{i=1}^{N_{el}/2} \int \psi_i^*(\mathbf{r}) \left(-\frac{1}{2} \nabla^2 \right) \psi_i(\mathbf{r}) d\mathbf{r} + E_{Coul}[n] + E_{ext}[n] + E'_{xc}[n] \quad (26)
 \end{aligned}$$

Approximations are sought for $E'_{xc}[n]$, which even though it now contains also contributions from kinetic energy, it is still called "Exchange-correlation functional" and from now on we will be writing it as $E_{xc}[n]$

2.10. Exchange correlational functional

The exchange-correlation (XC) functional is presented as the crucial, unknown component that renders the Kohn-Sham (KS) equations exact. It arises from the formal decomposition of the total electronic energy functional $E[n]$ within the Kohn-Sham framework. The total energy is expressed as :

$$E[n] = T_s[n] + E_{ext}[n] + E_H[n] + E_{xc}[n] \quad (27)$$

$E_{xc}[n]$ is the exchange-correlation functional, defined as the remaining part of the total energy that accounts for all non-classical many-body effects, including the difference between the true kinetic energy and $T_s[n]$, and all non-classical parts of the electron-electron interaction (exchange and correlation). It's given by:

$$E_{xc}[n] = (T[n] - T_s[n]) + (E_{ee}[n] - E_H[n]) \quad (28)$$

where $T[n]$ is the true kinetic energy functional of the interacting system, and $E_{ee}[n]$ is the true electron-electron interaction energy functional. The terms in the first parenthesis represent the kinetic energy correlation, and those in the second parenthesis represent the potential energy contributions from exchange and correlation beyond the classical Hartree term. The theoretical framework necessitates its existence to make the Kohn-Sham equations exact. The practical utility of DFT hinges entirely on finding accurate approximations for this functional. The simplest and most fundamental approximation discussed is the Local Density Approximation (LDA), which assumes that the exchange-correlation energy density at a given point \mathbf{r} depends only on the electron density at that point, treating the electron gas as locally homogeneous:

$$E_{xc}^{LDA}[n] = \int n(\mathbf{r}) \epsilon_{xc}(n(\mathbf{r})) d\mathbf{r} \quad (29)$$

where $\epsilon_{xc}(n)$ is the exchange-correlation energy per particle of a uniform electron gas of density n . This approximation provides a starting point for practical calculations, although its limitations for real, inhomogeneous systems are acknowledged, leading to the development of more sophisticated functionals discussed in later chapters.

2.11. Self-Consistent scheme of DFT

- The Kohn-Sham operator depends on the molecular orbitals which we seek.
- Therefore an iterative procedure needs to be used to find these orbitals.
- This procedure is often called a Self-Consistent Field (SCF) calculation.

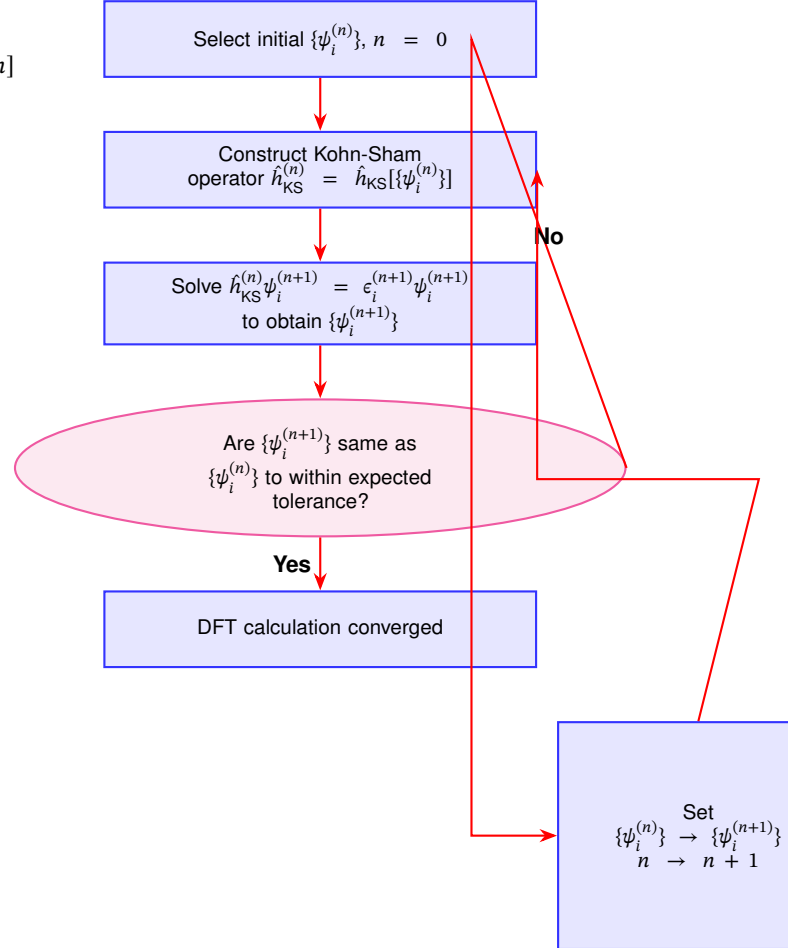


Figure 2. Self-Consistent Field (SCF) Iteration Scheme for DFT.

2.12. Hubbard Corrections DFT+U

Inspired by the Hubbard model, DFT+U method is formulated to improve the description of the ground state of correlated systems. The main advantage of the DFT+U method is that it is within the realm of DFT, thus does not require significant effort to be implemented in the existing DFT codes and its computational cost is only slightly higher than that of normal DFT computations. This "U" correction can be added to the local and semilocal density functionals offering LDA+U and GGA+U computational operations. The basic role of the U correction is to treat the strong on-site Coulomb interaction of localized electrons with an additional Hubbard-like term. The Hubbard Hamiltonian describes the strongly correlated electronic states (d and f orbitals), while treating the rest of the valence electrons by the normal DFT approximations. For practical implementation of DFT+U in computational chemistry, the strength of the on-site interactions is described by a couple of parameters: the on-site Coulomb term U and the site exchange term J. These parameters "U and J" can be extracted from ab initio calculations, but usually are obtained semiempirically. The implementation of the DFT+U requires a clear understanding of the approximations it is based on and a precise evaluation of the conditions under which it

can be expected to provide accurate quantitative predictions. The LDA+U method is widely implemented to correct the approximate DFT xc functional. The LDA+U works in the same way as the standard LDA method to describe the valence electrons, and only for the strongly correlated electronic states (the d and f orbitals), the Hubbard model is implemented for a more accurate modeling. Therefore, the total energy of the system (ELDA+U) is typically the summation of the standard LDA energy functional (E_{Hub}) for all the states and the energy of the Hubbard functional that describes the correlated states. Because of the additive Hubbard term, there will be a double counting error for the correlated states; therefore, a “double-counting” term (E_{dc}) must be deducted from the LDA’s total energy that describes the electronic interactions in a mean field kind of way

$$E_{LDA+U}[\rho(r)] = E_{LDA}[\rho(r)] + E_{Hub}[n_{mm}^{l\sigma}] - E_{dc}[n] \quad (30)$$

Therefore, it can be understood that the LDA+U is more like a substitution of the mean-field electronic interaction contained in the approximate xc functional. Nonetheless, the E_{dc} term is not uniquely defined for each system and various formulations can be applied to different systems. The most dominant of these formulations is the FLL formulation. It is based on the implementation of fully localized limit (FLL) on systems with more localized electrons on atomic orbitals. The reason for this formulation popularity is due to its ability to expand the width of the Kohn Sham (KS) orbitals and to effectively capture Mott localization. Based on this formulation, the LDA+U can be written as:

$$E_{LDA+U}[\rho(r)] + \sum_l [\frac{U^l}{2} \sum_{m,\sigma \neq m',\sigma'} n_m^{l\sigma} n_{m'}^{l\sigma'} - \frac{U^l}{2} n^l (n^l - 1)] \quad (31)$$

where $n_m^{l\sigma}$ are localized orbitals occupation numbers identified by the atomic site index l , state index m , and by the spin σ . In Eq. (31) the right-hand side second and third terms are the Hubbard and double-counting terms, specified in Eq. (32). The dependency on the occupation number is expected as the Hubbard correction is only applied to the states that are most disturbed by correlation effects. The occupation number is calculated as the projection of occupied KS orbitals on the states of a localized basis set:

$$n_{m,m'}^{l\sigma} = \sum_{k,v} f_{kv}^{\sigma} \langle \psi_{kv}^{\sigma} | \phi_m^{l\sigma} \rangle \langle \phi_m^{l\sigma} | \psi_{kv}^{\sigma} \rangle \quad (32)$$

where the coefficients f_{kv}^{σ} represent the occupations of KS states (labeled by k -point, band, and spin indices), determined by the Fermi-Dirac distribution of the corresponding single-particle energy eigen values. According to this formulation, the fractional occupations of localized orbitals is reduced, while assisting the Mott localization of electrons on particular atomic states.

Although the above approach described in Eq. (31) is able to capture Mott localization, it is not invariant under rotation of the atomic orbital basis set employed to define the occupation number of n in Eq. (32). This variation makes the calculations performed unfavorably dependent on the unitary transformation of the chosen localized basis set. Therefore, “rotationally invariant formulation” is introduced, which is unitary-transformation invariant of LDA+U. In this formulation, the electronic interactions are fully orbital dependent, and thus considered to be the most complete formulation of the LDA+U. However, a simpler formulation that preserves rotational invariance, which is theoretically based on the full rotationally invariant formulation, had proved to work as effectively as the full formulation for most materials. Based on the simplified LDA+U form, it has been customary to utilize, instead of the interaction parameter U , an effective U parameter: $U_{eff} = UJ$, where the “ J ” parameter is known as the exchange interaction term that accounts for Hund’s rule coupling. The U_{eff} is generally preferred because the J parameter is proven to be crucial to describe the electronic structure of certain classes of

materials, typically those subject to strong spin-orbit coupling.

2.13. Spin-Orbit Coupling

If we make the approximation that the spin-orbit term is small, then we can omit it in the radial equations for g and f and treat it by the perturbation theory. Then the dependency comes upon only the principle quantum number n and orbital angular momentum l and can be written in terms of the approximate functions, \tilde{g}_{nl} and \tilde{f}_{nl} , leading to,

$$-\frac{\hbar^2}{2M} \frac{1}{r^2} \frac{d}{dr} (r^2 \frac{d\tilde{g}}{dr}) + [V + \frac{\hbar^2}{2M} \frac{l(l+1)}{r^2}] \tilde{g}_{nl} - \frac{\hbar^2}{4M^2 c^2} \frac{dV}{dr} \frac{d\tilde{g}_{nl}}{dr} = \epsilon' \tilde{g}_{nl} \quad (33)$$

$$\tilde{f}_{nl} = \frac{\hbar}{2Mc} \frac{d\tilde{g}_{nl}}{dr} \quad (34)$$

with the normalization condition

$$\int (\tilde{g}_{nl}^2 + \tilde{f}_{nl}^2) r^2 dr = 1 \quad (35)$$

$$\mathbf{L} \cdot \boldsymbol{\sigma} \phi_{km} = -\hbar(1 + \kappa) \phi_{km} \quad (36)$$

Equation (33) is the scalar relativistic radial equation, which can be solved by the same techniques as the usual non-relativistic equation. The other equations can then be treated easily on the radial grid. Finally, the spin-orbit term can be included following the approach of MacDonald et al. Together with relation (36) the spin-orbit hamiltonian coupling the large components of the wavefunction has the form:

$$H_{SO} = \frac{\hbar^2}{2M^2 c^2} \frac{1}{r} \frac{dV}{dr} \mathbf{L} \cdot \boldsymbol{\sigma} \quad (37)$$

which can often be treated as a small perturbation. Since this term originates deep in the core near the nucleus where $\frac{1}{r} \frac{dV}{dr}$ is large, the present derivation of the spin-orbit term carries over from the atom to a solid or molecule.

2.14. LOPTICS(Theory)

The imaginary part is determined by a summation over empty states using equation:

$$\epsilon_{\alpha\beta}^{(2)}(\omega) = \frac{4\pi^2 e^2}{\Omega} \lim_{q \rightarrow 0} \frac{1}{q^2} \sum_{c,v,k} 2\omega_k \delta(\epsilon_{ck} - \epsilon_{vk} - \omega) I \quad (38)$$

$$I = \langle u_{ck+e_{\alpha}q} | v_{vk} \rangle \langle u_{vk} | u_{ck+e_{\beta}q} \rangle \quad (39)$$

here the indices c and v refer to conduction and valence band states respectively, and u_{ck} is the cell periodic part of the orbitals at the k -point \mathbf{k} . The real part of the dielectric tensor $\epsilon^{(1)}$ is obtained by the usual Kramers-Kronig transformation

$$\epsilon_{\alpha\beta}^{(1)}(\omega) = 1 + \frac{2}{\pi} P \int_0^{\infty} \frac{\epsilon_{\alpha\beta}^{(2)}(\omega') \omega'}{\omega'^2 - \omega^2 + i\eta} d\omega' \quad (40)$$

where P denotes the principle value.

Note that local field effects, i.e. changes of the cell periodic part of the potential are neglected in this approximation. These can be evaluated using either the implemented density functional perturbation theory (LEPSILON=.TRUE.), or the GW routines.

The method selected using `LOPTICS=.TRUE.` requires an appreciable number of empty conduction band states. Reasonable results are usually only obtained, if the parameter `NBANDS` is roughly doubled or tripled in the INCAR file with respect to the VASP default. Furthermore it is emphasized that the routine works properly even for HF and screened exchange type calculations and hybrid functionals. In this case, finite differences are used to determine the derivatives of the Hamiltonian with respect to \mathbf{k} .

Note that the number of frequency grid points is determined by the parameter NEDOS. In many cases it is desirable to increase this parameter significantly from its default value. Values around NEDOS=2000 are strongly recommended.

VASP poses multiple other routines to calculate the frequency dependent dielectric function. Specifically, one can use ALGO = TDHF (Casida/BSE calculations), ALGO = GW (GW calculations) and ALGO = TIMEEV (Time Evolution: apply a delta kick and follow the induced dipoles). Compared to LOPTICS=.TRUE., all those routines have the advantage to include effects beyond the independent particle approximation, however, they are usually also much more expensive than LOPTICS=.TRUE.

2.14.1. Spectral Broadening

The dielectric function calculated with LOPTICS includes broadening due to the smearing method ISMEAR and the Lorentzian broadening due to the complex shift in the Kramers-Kronig transformation. For example, the combination of LOPTICS=.TRUE. and ISMEAR=0 produces the dielectric function broadened by a Gaussian with the width SIGMA and a Lorentzian with the width CSHIFT. To avoid using two different broadening methods imultaneously and only include the Lorentzian broadening, one should set SIGMA to a much smaller value than CSHIFT.

3. RESULTS

3.1. Lattice Parameters

Lattice Type - p

Space group name - p 1

Space group number - 1

Table 1. Pristine Structure

a	b	c	α	β	γ
3.43283	3.43283	18.23249	90.0000	90.0000	120.0000

Unit-cell volume = 186.071849 Å³ [DataSource : VESTA]

	Element	Site	x	y	z	Occ.
1	W	W1	0.00000	0.00000	0.50607	1.000
2	Se	Se1	0.66667	0.33333	0.59521	1.000
3	Te	Te1	0.66667	0.33333	0.40354	1.000

Table 2. Structure parameters including element, site, coordinates, occupancy and thermal parameter = 0

3.2. uniaxial strain data

No.	a	b	c	α	β	γ
a-4%	3.23620	3.37099	9.60611	90.0000	90.0000	120.00
b-4%	3.37104	3.23615	9.60611	90.0000	90.0000	120.00
a-3%	3.26991	3.37099	9.60611	90.0000	90.0000	120.00
b-3%	3.37104	3.26986	9.60611	90.0000	90.0000	120.00
a-2%	3.30362	3.37099	9.60611	90.0000	90.0000	120.00
b-2%	3.37104	3.30357	9.60611	90.0000	90.0000	120.00
a-1%	3.33733	3.37099	9.60611	90.0000	90.0000	120.00
b-1%	3.37104	3.33728	9.60611	90.0000	90.0000	120.00

3.3. BANDS

For the band structure with 4% strain has an energy range of 0.0 to 3.0 eV. The band structure appears to have a direct band gap with VBM (Valence band maxima) and conduction band minimum (CBM) are at the same k-point) or an indirect bandgap (if they are at different k-points). The exact nature depends on the k-point locations. The

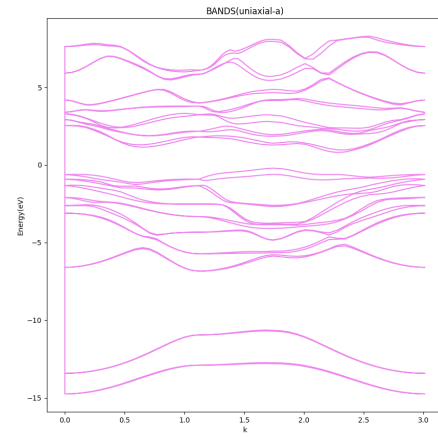


Figure 3. Electronic Band Structure uniaxial-a 4% strain

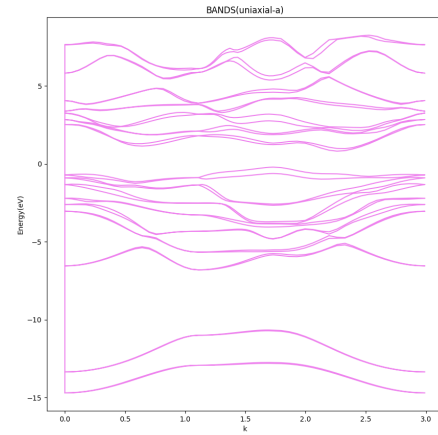


Figure 4. Electronic Band Structure uniaxial-a 3% strain

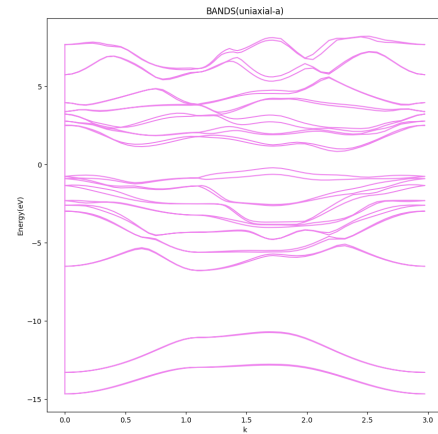


Figure 5. Electronic Band Structure uniaxial-a 2% strain

	Element	Site	x	y	z	Occ.
1	W(a-4%)	W1	0.99674	0.99685	0.51048	1.000
2	Se(a-4%)	Se1	0.66848	0.33508	0.68311	1.000
3	Te(a-4%)	Te1	0.66811	0.33474	0.31124	1.000
4	W(b-4%)	W1	0.00315	0.00326	0.51048	1.000
5	Se(b-4%)	Se1	0.66492	0.33152	0.68311	1.000
6	Te(b-4%)	Te1	0.66526	0.33189	0.31124	1.000
7	W(a-3%)	W1	0.99787	0.99791	0.51043	1.000
8	Se(a-3%)	Se1	0.66784	0.33447	0.68241	1.000
9	Te(a-3%)	Te1	0.66763	0.33429	0.31198	1.000
10	W(b-3%)	W1	0.00210	0.00214	0.51043	1.000
11	Se(b-3%)	Se1	0.66553	0.33216	0.68241	1.000
12	Te(b-3%)	Te1	0.66571	0.33237	0.31198	1.000
13	W(a-2%)	W1	0.00210	0.00214	0.51043	1.000
14	Se(a-2%)	Se1	0.66553	0.33216	0.68241	1.000
15	Te(a-2%)	Te1	0.66571	0.33237	0.31198	1.000
16	W(b-2%)	W1	0.00105	0.00106	0.51039	1.000
17	Se(b-2%)	Se1	0.66614	0.33280	0.68170	1.000
18	Te(b-2%)	Te1	0.66614	0.33280	0.31272	1.000
19	W(a-1%)	W1	0.00000	0.00000	0.50878	1.000
20	Se(a-1%)	Se1	0.66667	0.33333	0.64930	1.000
21	Te(a-1%)	Te1	0.66667	0.33333	0.34674	1.000
22	W(b-1%)	W1	0.00000	0.00000	0.50607	1.000
23	Se(b-1%)	Se1	0.66667	0.33333	0.59521	1.000
24	Te(b-1%)	Te1	0.66667	0.33333	0.40354	1.000

Table 3. Structure parameters including element, site, coordinates, occupancy and thermal parameter

strain of 4% likely causes significant distortion in the lattice, leading to noticeable changes in the band dispersion. The bands may show flattening or shifting, indicating altered electronic properties. The large strain could introduce band splitting or degeneracy lifting due to reduced symmetry. For the band structure with 3% strain has an energy range of 0.5eV to 3.0eV. Compared to the 4% case, the bands may appear less distorted, suggesting a partial relaxation of the lattice. Depending on the compressive strain along one of the direction thus the bandgap is larger as the compressive strain typically reduces the interatomic distance, increasing orbital overlap. For compressive strain (-a direction), the bandgap of WSeTe is expected to increase with higher strain (4% > 1%), consistent with your band structures. This is useful for strain-tuning the material for specific applications (e.g., larger gap for higher voltage optoelectronics). For the application of 2% strain the energy range extends from 0.5eV to 3.0eV. The

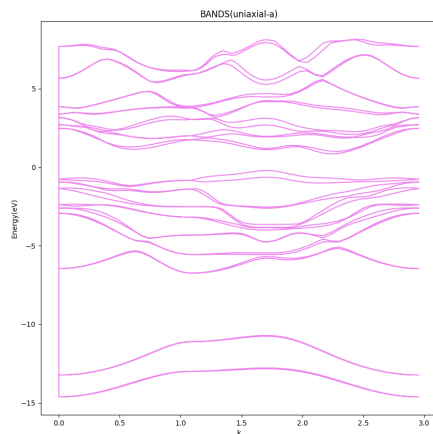


Figure 6. Electronic Band Structure uniaxial-a 1% strain

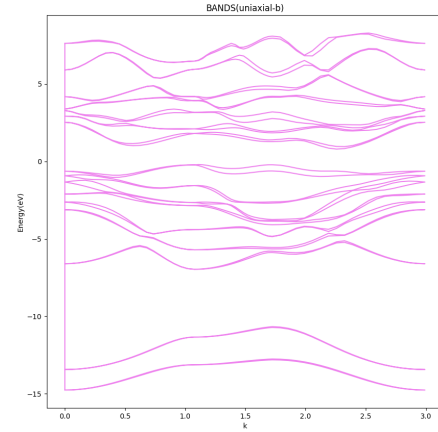


Figure 7. Electronic band structure uniaxial-b 4% strain

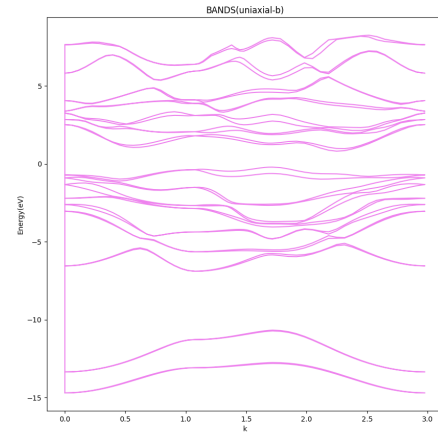


Figure 8. Electronic band structure uniaxial-b 3% strain

bands are likely closer to the equilibrium (unstrained) structure, with less pronounced distortion. The bandgap may trend toward the intrinsic value of WSeTe, suggesting that 2% strain is a moderate perturbation. The symmetry of the bands might be partially restored compared to higher strains. For the 1% strain the energy range remains the same as the previous cases. This is the smallest strain, so the band structure should resemble the unstrained monolayer most closely. The bandgap and dispersion are likely near their natural values, with minimal strain-induced effects. Any splitting or shifting of bands is subtle, indicating that 1% strain has a minor impact.

For the uniaxial-b compressive straining we have for the 4% strain the Bandgap E_g is expected to increase significantly due to strong compressive strain. Compression reduces interatomic distances, increasing orbital overlap and pushing conduction bands higher/valence bands lower. In terms of the Band dispersion the flattening of bands near the K point \rightarrow Higher effective mass for electrons/holes. Possible splitting of degenerate states (e.g., at the VBM) due to symmetry reduction. Larger $E_g \rightarrow$ Blue-shifted absorption/emission (e.g., for LEDs or photodetectors). Reduced carrier mobility due to heavier masses. For the compressive 3% strain the bandgap is slightly smaller than 4% but still larger than unstrained case. Regarding the Band Dispersion the partial recovery of curvature \rightarrow Effective mass decreases vs. 4%. Less splitting than 4% suggesting partial symmetry restoration. In terms of the Optical Implications moderate blue-shift in optical transitions. Carrier transport improves compared to the 4%

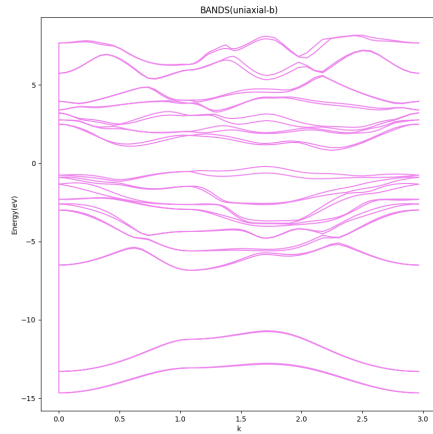


Figure 9. Electronic band structure uniaxial-b 2% strain

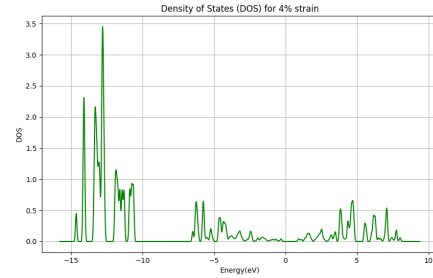


Figure 11. DOS for uniaxial-a under 4% strain

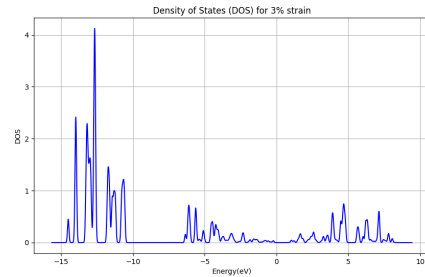


Figure 12. DOS for uniaxial-a under 3% strain

case. The 2% compressive strain ensures the bandgap to be closer to the unstrained value but still slightly widened. For the Band Dispersion, near the parabolic bands at $K \rightarrow$ Effective mass approaches pristine values. Degeneracies are mostly preserved. Optical implications involve minimal shift in absorption edge. High carrier mobility retained. For the 1% compressive strain bandgap is the smallest in the series of other compressed structures, nearly identical to the unstrained WSeTe. Band dispersion involve sharp, parabolic bands \rightarrow Light carriers (low effective mass). No observable splitting (the entire symmetry is preserved). Optical implications involve no significant change in optical properties compared to the unstrained cases. Optimal for high speed optoelectronics.

3.4. DOS

General observations include valence band range from -15 eV to 0 eV dominated by the Se/Te p -orbitals and W d -orbitals. The conduction band has its range in 0 eV to 10 eV, primarily W d -orbitals with minor Se/Te contributions. The Fermi Level is likely to be at 0 eV. The compressive uniaxial strain along one direction modifies orbital overlap, shifting states and altering hybridization. Analyzing based on strain applications, for 4% strain the valence band features include broadening near -5 eV to 0 eV \rightarrow Enhanced W d -Se/Te p hybridization due to reduced interatomic distances. Possible splitting of degenerate states from symmetry breaking. The Conduction band features include shifted **CB minima** (higher energy) \rightarrow Larger

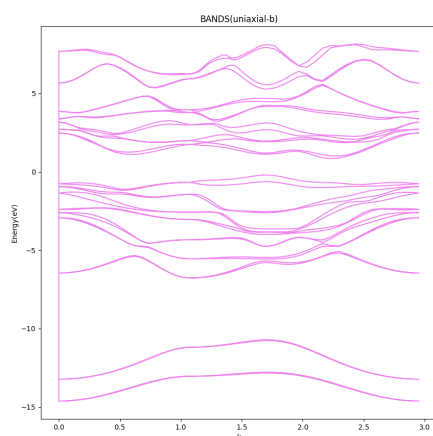


Figure 10. Electronic band structure uniaxial-b 1% strain

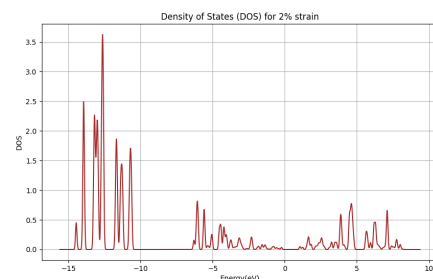


Figure 13. DOS for uniaxial-a under 2% strain

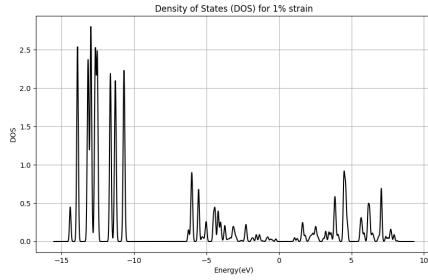


Figure 14. DOS for uniaxial-a under 1% strain

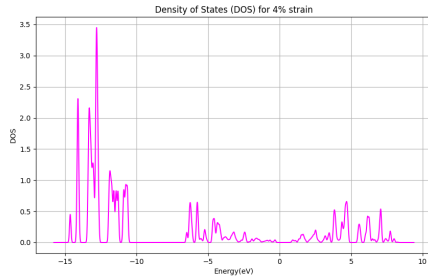


Figure 15. DOS for uniaxial-b under 4% strain

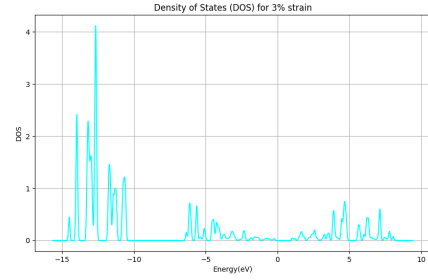


Figure 16. DOS for uniaxial-b under 3% strain

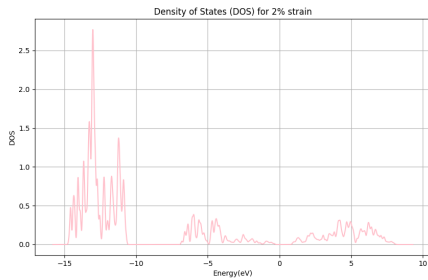


Figure 17. DOS for uniaxial-b under 2% strain

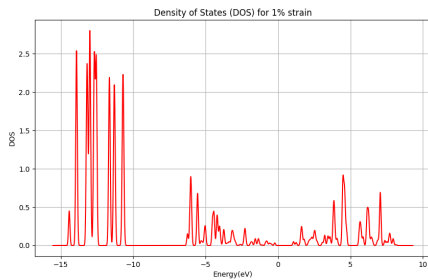


Figure 18. DOS for uniaxial-b under 1% strain

bandgap, consistent with band structure analysis. Reduced DOS near EF \rightarrow Fewer available states for carriers. Noticeable feature includes the highest intensity (~ 3.5) suggesting strong localization of states. For the 3% strain interms of the Valence Band Features include less peak broadening compared to the 4% case and it is suggestive that it involved partial relaxation of hybridization. The splitting was retained but with a lower intensity (~ 2.5 vs. 3.5 in 4%). The conduction band features include a shift of minima less than 4% and thus the smaller bandgap increase. Smoother density of states near EF suggests improved carrier availability. At 2% strain the valence band features have sharper peaks near $-5\text{eV} \rightarrow$ restored orbital degeneracy. The localization gets reduces at the DOS intensity reduces to ~ 2.0 . The Conduction band features its minima closer to pristine positions \rightarrow Bandgap approaches unstrained value. The increased density of states near the EF reinforces the fact of better conductivity. The 1% strain case for the features of the Valence band includes near-pristine sharp peaks and therefore minimal strain-induced hybridization changes. The lowest intensity is observed ~ 1.5 , thus delocalized states. The features of the conduction band include its minima aligned with the unstrained case, thus the smallest bandgap. High DOS near EF suggests the fact of optimal carrier transport.

3.5. Phonon Enthalpy

The energy capacity increases monotonically, indicating an increased disorder and accessible phonon modes with temperature. Entropy increases monotonically, indicating an increase in the Heat Capacity (C_V) is observed at low temperatures, saturating near 75 J/K/mol by $\sim 700\text{K}$, consistent with Dulong-Petit limit. Due to the strain softened phonons come into play causing a reduction of the deby temperature, thus increasing C_V at low T - consistent with the observed plot shape.

The 4% strain which is the strongest compression, for the Valence Band (VB) features include broader peaks near -10eV to $-5\text{eV} \rightarrow$ implying strong **W d-Te/Se p hybridization** (Te likely more affected due to large atomic size). Splitting occurs at -3eV and hence symmetry breaking lifts degeneracies. The Conduction Band (CB) features minima shifted CB minima (higher energy) hence larger bandgap. Reduced DOS near the fermi level observed indicates fewer conductive states. Highest DOS intensity (~ 3.5) indicates localized

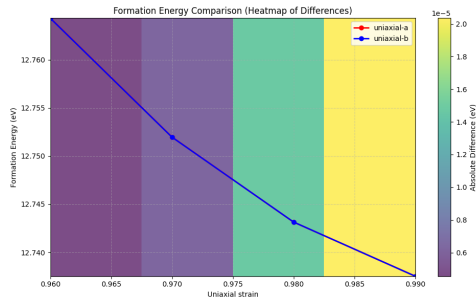


Figure 19. Formation Energy(eV)

states. For the 3% strain the VB features less broadening than 4% hence partial relaxation of strain effects. The splitting is retained but with lower intensity (~ 2.5). The CB features shift less pronounced than 4% thus moderate bandgap increases. Smoother DOS near Fermi level (EF) ensures better carrier availability. For the 2% strain the VB shows sharp peaks near -5eV thus restoring the orbital degeneracy. The Density of States intensity drops to ~ 1.5 hence reducing localization. The CB features minima closer to pristine positions hence bandgap approaches unstrained value. Increased DOS near the Fermi Level provides the improved conductivity. Finally for the weakest compression 1% we have the VB featuring near-pristine sharp peaks thus minimal hybridization changes. Lowest DOS intensity (~ 1.0) assuring delocalized states. The CB features its minima aligning with the unstrained case thus smallest bandgap is observed. High DOS near Fermi Level (EF) provides optimal carrier transport.

3.6. Formation Energy

This is some introductory text for the subsection, leading up to the table. The following table presents key experimental results.

Table 4. Formation energy in uniaxial-a under compressive strain

strain	E_N (eV)	Number of atoms
1%	-21.90092513	3
2%	-21.88404675	3
3%	-21.85760243	3
4%	-21.82057757	3

Table 5. Formation energy in uniaxial-b under compressive strain

strain	E_N (eV)	Number of atoms
1%	-21.90091147	3
2%	-21.88406539	3
3%	-21.85755824	3
4%	-21.82051652	3

For **W** the E_N is equal to -26.49650013eV with 2 atoms in the unit cell being optimized while for **Se** it is -225.80239987 with the number of atoms in the unit cell optimized is 64. **Se** has its formation energy equal to -9.78425041 with 3 atoms in the unit cell. For the uniaxial compressive strain along a direction we have the formation energy for the **1%, 2%, 3% and the 4% cases are** : 12.73752099eV, 12.74314712eV, 12.75196189eV, 12.76430351eV. Similarly for the compressive strain along the b direction have the following energies for similar 12.73752554eV, 12.7431409eV, 12.75197662eV, 12.76432386eV

3.7. Phonon Enthalpy

Free Energy (F) is likely the highest among all strains due to strong lattice distortion, indicating reduced thermodynamic stability at high temperatures. **Entropy (S)** is expected to be lower than lower strains

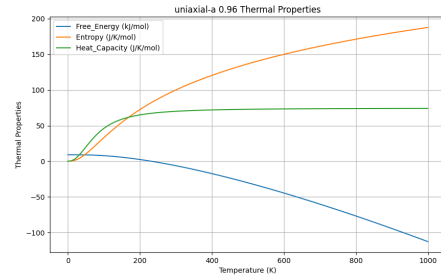


Figure 20. Thermal Properties uniaxial-a for 4%

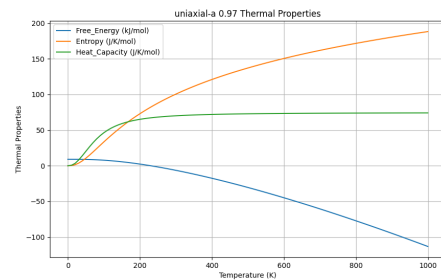


Figure 21. Thermal Properties uniaxial-a for 3%

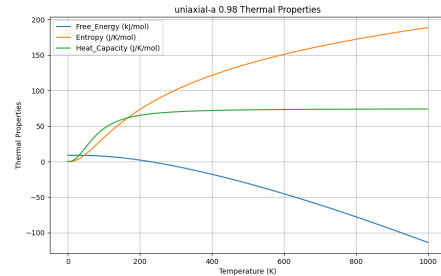


Figure 22. Thermal Properties uniaxial-a for 2%

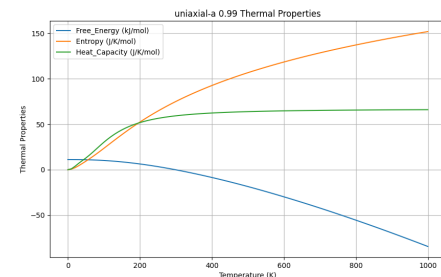


Figure 23. Thermal Properties uniaxial-a for 1%

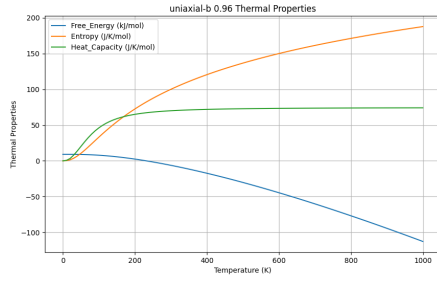


Figure 24. Thermal properties uniaxial-b for 4% strain

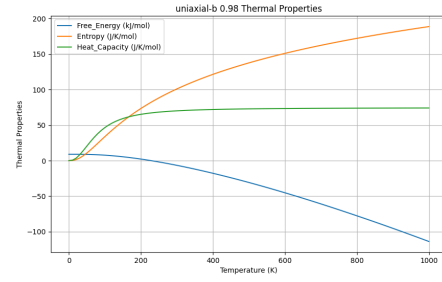


Figure 26. Thermal properties uniaxial-b for 2% strain

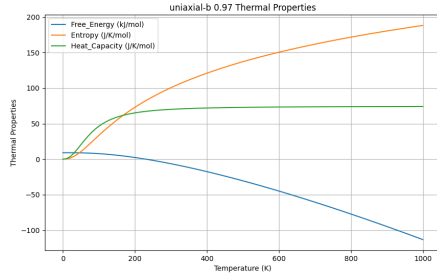


Figure 25. Thermal properties uniaxial-b for 3% strain

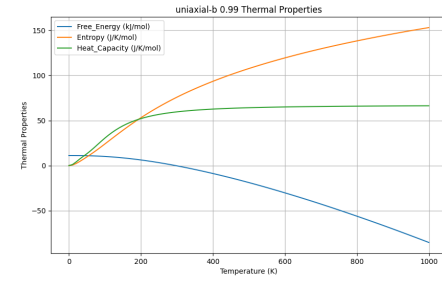


Figure 27. Thermal properties uniaxial-b for 1% strain

due to restricted atomic vibrations from compression. Reduced disorder implies fewer accessible vibrational states. **Heat Capacity (C_V)** is lower than the pristine or low-strain cases (stiffened phonon modes limit energy absorption). The heat capacity flattens at high T , suggesting saturation of vibrational modes. Implications from the above observed trend involve poor thermal stability at high temperatures and reduced thermal conductivity (lower S and C_V limit phonon transport).

For the 3% compressive strain case the F is moderate compared to 4% strain, but still it is elevated compared to the 1-2% strain. **Entropy (S)** is higher than 4% strain but lower than 1-2% which causes partial recovery of vibrational modes. **Heat Capacity C_V** gives off intermediate values with gradual rise in comparison to the temperature. The heat capacity shows off less saturation than the 4% strain. Hence the above study gives the implications of balanced stability for moderate-temperature applications and improved thermal transport over the 4% strain. For the 2% compressive strain the free energy F approaches near pristine values cause of the minimal strain penalty. The entropy shows near maximum for strained cases and hence more vibrational freedom. The C_V is close to the unstrained monolayer values hence efficient in energy storage. Thus the implications for the following strain provides the evidence that the corresponding case makes it optimal for high temperature devices (e.g., power electronics) and has high thermal conductivity (phonons are less restricted). For the 1% compressive strain the F being the lowest among the strained cases hence most thermodynamically stable. The S is highest, hence maximized disorder from minimal lattice constraints. The heat capacity C_V matches with the unstrained WSeTe hence no phonon mode suppression.

For compressive strain 4% in another uniaxial direction the free energy (F) is highest among all cases, indicating significant lattice distortion that reduces thermodynamic stability. Entropy (S) is lowest due to restricted atomic vibrations from strong compression, limiting phonon modes. Heat capacity C_V has the lowest values, showing reduced energy absorption capacity as phonon modes stiffen. For strain 3% the free energy is slightly lower than 4%, suggesting partial relaxation of lattice constraints. Entropy moderately increases compared to the 4% case, reflecting some recovery of vibrational freedom. The Heat capacity has intermediate values, indicating par-

tial restoration of phonon contributions to energy storage. The 2% compressive strain has its free energy approaching near unstrained levels, showing minimal impact on thermodynamic stability. Entropy is high in this case and close to the pristine values, as most vibrational modes are restored. Heat capacity near unstrained performance is efficient for thermal management. The 1% compressive strain has F lowest, indicating the system thermodynamically most stable. The entropy is highest with maximal vibrational disorder, akin to the unstrained monolayer. The C_V is optimal, matching unstrained WSeTe, ideal for high-temperature applications. Practical implications include that for **High Strain (4%)** is suitable for applications where electronic properties are prioritized over thermal performance, and the **Low strain (1-2%)** is ideal for devices requiring efficient thermal management, such as high-power electronics and thermoelectric materials.

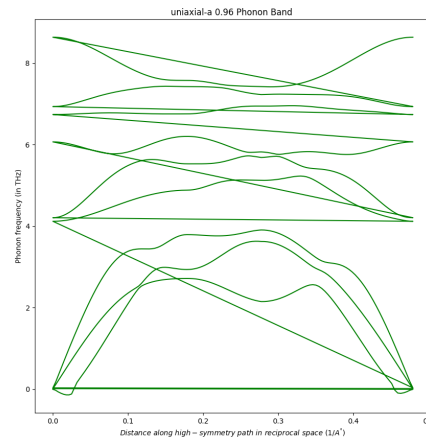


Figure 28. Phonon dispersion uniaxial-a under 4%

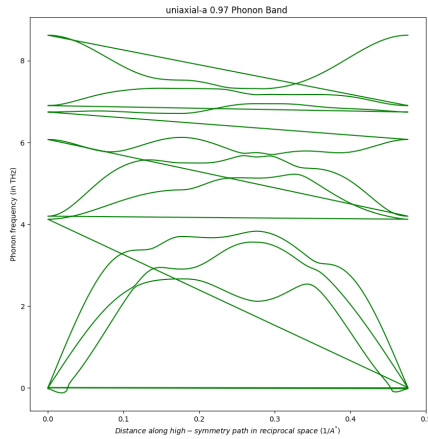


Figure 29. Phonon dispersion uniaxial-a under 3%

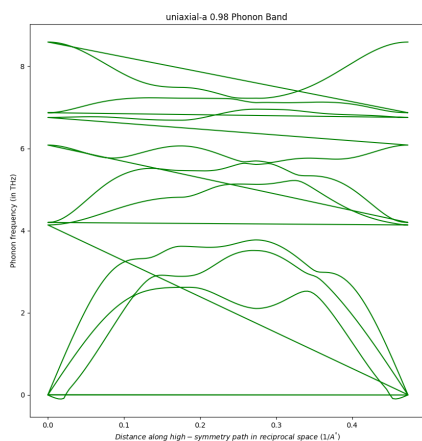


Figure 30. Phonon dispersion uniaxial-a under 2%

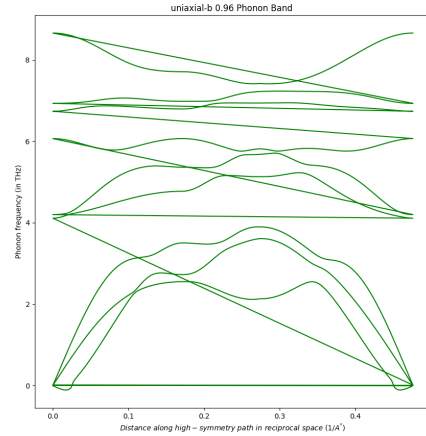


Figure 31. Phonon dispersion uniaxial-b under 4%

3.8. Phonon Dispersion

For the compressive 4% strain optical modes are W-dominated hence shifted to higher frequencies (6-10 THz) due to bond stiffening. Acoustic modes (Se/Te-dominated) hence flattened near Γ point (0-2 THz) indicating suppressed sound velocity. Band gaps are likely visible between acoustic and optical branches (~3-5 THz) due to strain-induced decoupling. Implications from the above study relative to thermal conductivity (κ) is severely reduced, flattened acoustic branches hinder heat transport. Soft modes near Γ/M points may indicate pre-transition states reinforcing dynamical stability. Anisotropy is also observed from directional hardening of LA/TA modes along direction of the application of the strain. For the 3% compressive strength optical modes are slightly lowered (5-8 THz) compared to the 4% strain, showing partial relaxation. In terms of the acoustic modes steeper slope near Γ (0-3 THz) means improved sound velocity. Band gaps are narrower than 4% strain (~2-4 THz), suggesting better phonon coupling. Implications for κ is a moderate recovery as acoustic modes regain dispersion. For stability no soft modes expected hence stable lattice. The phonon lifetimes are longer than the 4% strain due to reduced anharmonicity. For the 2% compressive strength the optical modes are near pristine (4-7 THz) with restored degeneracy. Acoustic modes have linear dispersion near Γ (0-4 THz) hence referring to high sound velocity. Band gaps are minimal or absent thus strong acoustic-optical phonon hybridization is observed. Thermal conductivity is high and so efficient heat carried by acoustic phonons are observed. Ideal for high-power/flexible electronics.

The compressive strain of 4% have optical modes W-dominated which for W is expected to shift to 5-9 THz (slightly lower than uniaxial-a due to Te's mass effect). Possible splitting of degenerate modes at K/ Γ points from symmetry breaking. Acoustic modes are Te-dominated, it is flattened near Γ (0-1.5 THz), hence severely suppressing the sound velocity. TA/LA branches may show anomalous curvature due to Te-Se bond distortion. Band gaps are larger than uniaxial-a case (~4-6 THz) thus stronger phonon decoupling. There is a high risk of imaginary frequencies and structure instability. The thermal conductivity is worse than the compressive strain application in uniaxial-a case as Te-acoustic modes are critical for heat transport. Anisotropy is observed as a result of extreme directionality-phonons along uniaxial-b are frozen while may retain some mobility. The 3% compressive strain shifts the optical modes to 4-7 THz which is softened compared to the 4% strain. Partial recovery of degeneracy at high-symmetry points. Acoustic modes manifest steeper slopes near Γ (0-2.5 THz) which is improved but still limited sound velocity. TA branch may remain flatter than LA due to Te's shear sensitivity. Band gaps reduced to ~2-4 THz which is better phonon coupling than 4%. Thermal conduc-

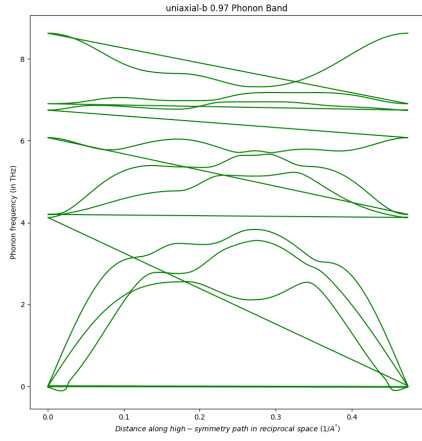


Figure 32. Phonon dispersion uniaxial-b under 3%

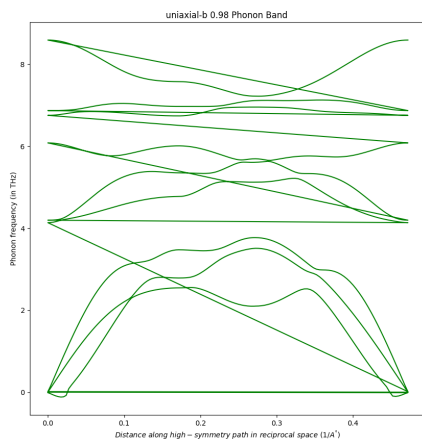


Figure 33. Phonon dispersion uniaxial-b under 2%

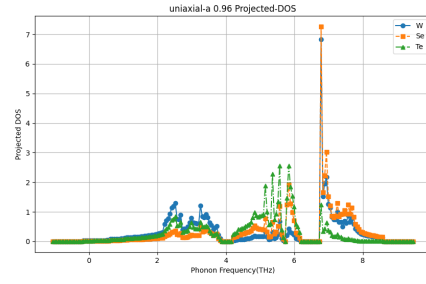


Figure 34. Projected Phonon Density of States uniaxial-a 4% strain

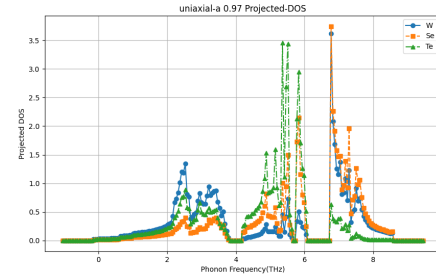


Figure 35. Projected Phonon Density of States uniaxial-a 3% strain

tivity although poor but better than the 4% case. Phonon lifetimes are longer than the 4% case due to reduced anharmonic scattering. The 2% compressive strain has its optical modes near pristine frequencies (3-6 THz) and restored degeneracies are also observed at K/Γ. Acoustic modes show linear dispersion and hence healthy sound velocity near Γ (0-3.5 THz). TA/LA branches show minimal strain effects. Band gaps are minimal or absent thus proving for the strong acoustic-optical hybridization.

Comparative study reveals the Te-driven catastrophe under uniaxial-b strain, Te acoustic mode fails first, causing disproportionate thermal degradation compared to the uniaxial-a strain. For strains $>3\%$ along uniaxial-b irreversibly damages phonon transport causing it a hard limit for device design. Anisotropy in thermal conductivity for uniaxial-a κ_a or uniaxial-b κ_b peaks at $\sim 2.5\times$ under 4% strain.

3.9. Projected Phonon DOS

For the 4% strain case the frequency range for Tungsten dominates within 5-10 THz resulting in further stiffened optical modes due to extreme compression. For the Te being suppressed below 3 THz, acoustic modes are hindered by the lattice distortion. The PDOS intensity for W has sharp peaks implying for strong localization. For the Se/Te we observe flattened peaks referring to phonon freezing in low-frequency regimes. The possible frequency gap between W and Se/Te modes are due to the strain-induced decoupling. Implications of the above analysis in terms of thermal conductivity is the high frequency

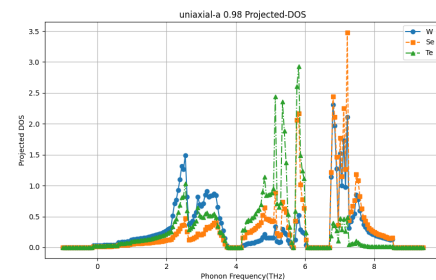


Figure 36. Projected Phonon Density of States uniaxial-a 2% strain

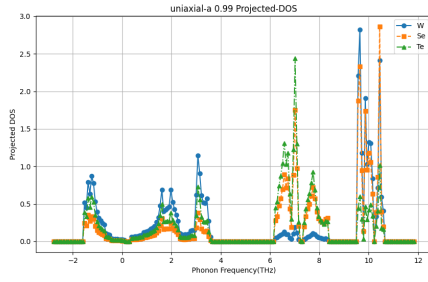


Figure 37. Projected Phonon Density of States uniaxial-a 1% strain

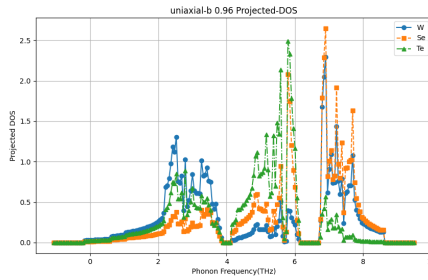


Figure 38. Projected Phonon Density of States uniaxial-b 4% strain

W modes scatter heat while the Se/Te modes are inactive. The Thermal conductivity is comparable to the amorphous materials. Large Gruneisen parameters suggest strong phonon phonon scattering. For the 3% compressive strain the frequency range is 0-8 THz (typical for acoustic/optical phonons). W dominates higher frequencies (4-8 THz) indicating strong involvement in optical phonon modes. Se/Te contribute more to low-frequency modes (0-4 THz), especially Te due to its larger mass. Density of states has its intensity peak at ~3.5 (W) implying strong localization of high energy phonons. Se/Te peaks below 2.0 refer to the delocalized acoustic modes. Implications involve thermal conductivity reduced due to suppress low frequency (Se/Te) modes. High-frequency W modes may scatter heat-carrying phonons. Compression stiffens W-dominated modes, widening the frequency gap between W and Se/Te. The 2% compressive strain share the same frequency range as the 3% but with shifted peaks. The orbital contributions involve W peaks shift slightly slower (3-7 THz), suggesting softened optical modes. Se/Te has increased intensity in 2-4 THz range implying enhanced acoustic phonon activity. The Projected DOS for W peaks at ~3.0 compared to 3.5 in 3% straining case hence reduced localization. The Se/Te peaks near 1.5 thus proving for more balanced phonon distribution. The 1% compressive strain unlike the other straining cases has its frequency range extended due to minimal strain distribution (0-12 THz). Orbital contributions for W peaks spread across 4-10 THz hence restoring degeneracy in optical modes. Se/Te has its orbital contributions dominating below 4 THz, with Te showing stronger low frequency peaks. The Projected DOS for W peaks below 2.0 thus proving for high delocalization. While for Se/Te peaks at ~1.0 thus maximizing acoustic phonon contributions. Implications involve high thermal conductivity and minimal phonon scattering.

The 4% compressive strain for the uniaxial-b case has its frequency range in 0-8 THz similar to the previous uniaxial strain case but with stronger Te effects. Orbital contributions involve Te dominating at low frequencies (0-3 THz) due to its large mass and strain-sensitive bonds. Se provide minimal contribution more likely overshadowing Te. W have high-frequency modes (5-8 THz) are highly localized. Projected DOS intensity peaks at very low frequencies (<2 THz) implying strong acoustic phonon suppression. W peaks near 4.0 thus implying extreme localization of optical modes. For 3% compressive strain the frequency range is shifted compared to the 4% case. Orbital

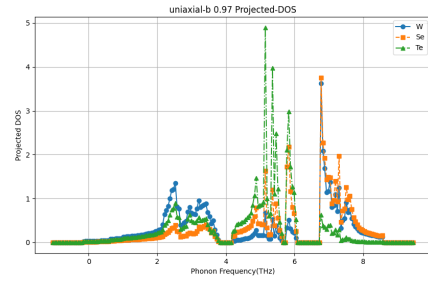


Figure 39. Projected Phonon Density of States uniaxial-b 3% strain

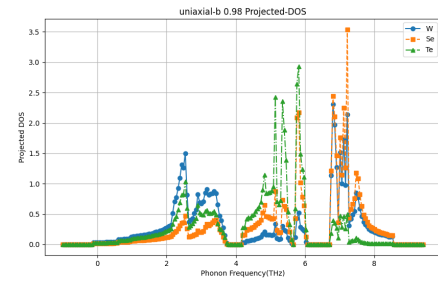


Figure 40. Projected Phonon Density of States uniaxial-b 2% strain

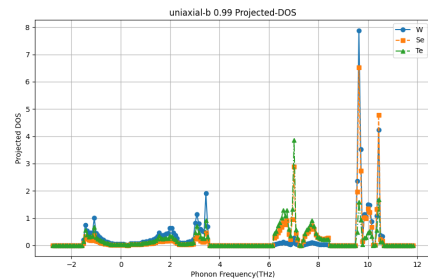


Figure 41. Projected Phonon Density of States uniaxial-b 1% strain

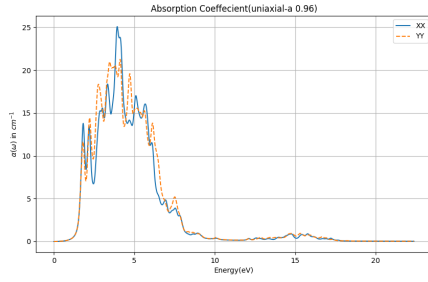


Figure 42. Absorption spectra uniaxial-a for 4% strain

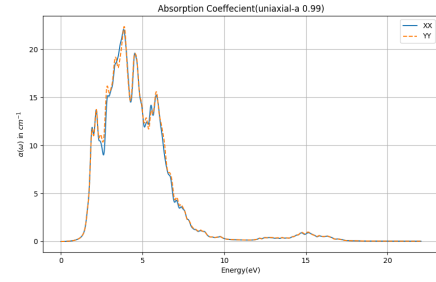


Figure 45. Absorption spectra uniaxial-a for 1% strain

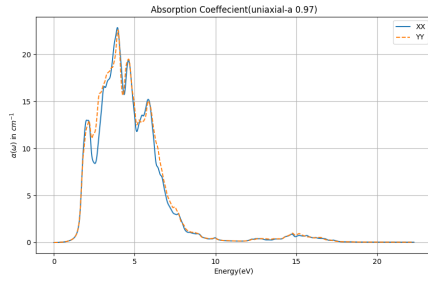


Figure 43. Absorption spectra uniaxial-a for 3% strain

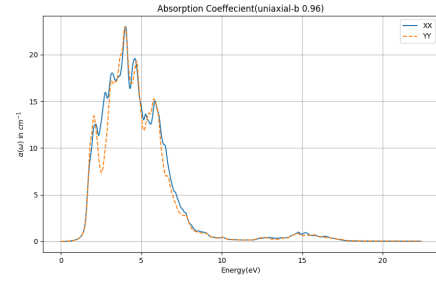


Figure 46. Absorption spectra uniaxial-b for 4% strain

3.10. Absorption Spectra

For the 4% strain case strong optical anisotropy is observed. The absorption coefficients in either direction show significant differences. Absorption intensity peaks at $\sim 25 \text{ cm}^{-1}$. Broad and sharp peaks in the 3-6 eV range suggest strong interband transitions. Low onset energy ($\sim 1.2 \text{ eV}$), implying a narrow band gap or red shift in optical absorption. Indications of strain induced enhancement of optical transitions are observed in the visible UV region. The 3% strain case demonstrates reduced anisotropy for the XX and YY curves are getting closer in shape and intensity. Peak positions slightly shift, and intensities are still relatively high but somewhat less sharp than in the 4% case. Indicates reduction in transition matrix element asymmetry under decreasing strain. For the 2% case in uniaxial-a compressive strain further convergence between XX and XY is observed. Very similar absorptions profiles are encountered with small residual anisotropy. The peak becomes smoother and slightly lower in intensity. Optical properties are becoming more isotropic and strain effects are diminishing. The 1% case demonstrates near-isotropic optical behavior with the XX and XY are almost completely overlapping. Lowest peak intensity among all cases, with reduced sharpness and fewer fine structures. Implications of a recovery toward the unstrained electronic band structure, with reduced influence of compressive stress.

Absorption spectra analysis for compressive strain 4% along uniaxial-b involve XX and XY components as distinguishable. There's moderate

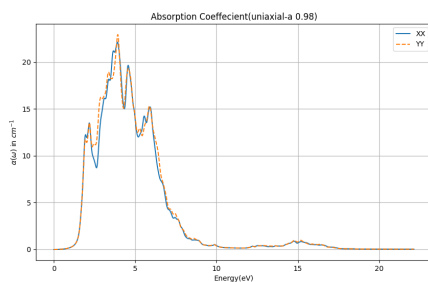


Figure 44. Absorption spectra uniaxial-a for 2% strain

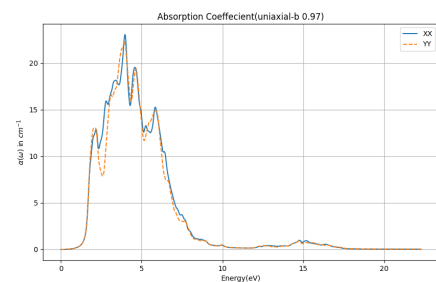


Figure 47. Absorption spectra uniaxial-b for 3% strain

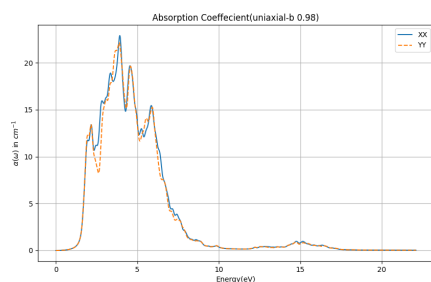


Figure 48. Absorption spectra uniaxial-b for 2% strain

- <https://www.math.purdue.edu/~kdatchev/dftintro.pdf>
- <https://arxiv.org/pdf/cond-mat/0211443>
- <https://www.southampton.ac.uk/assets/centresresearch/documents/com>
- <https://www.southampton.ac.uk/assets/centresresearch/documents/com>
- <https://www.intechopen.com/chapters/58999>

anisotropy in the absorption spectra, but less than in the uniaxial-a case. The absorption peaks reach $\sim 23 \text{ cm}^{-1}$ in the visible-UV region (3-6 eV). The peak splitting in the 4-6 eV range indicates strong electronic transitions possibly modified by symmetry breaking due to strain. Low onset energy of absorption ($\sim 1.2 \text{ eV}$) implies a smaller band gap, similar to uniaxial-a strain at the same magnitude. YY component slightly lags behind XX in terms of intensity across most of the spectrum. For the 3% strain absorption peaks remain strong, though slightly reduced compared to the 4% case. The XX-XY anisotropy is further reduced, but still visible, especially in the 4-6 eV range. There is peak alignment between XX and XY curves, suggesting that symmetry is being gradually restored as strain reduces. The structure of spectrum is preserved, indicating minimal deformation of the electronic band structure under this level of compression. For the 2% strain case along the uniaxial-b the XX and XY components nearly overlap, showing very weak anisotropy. Slight decrease in absorption intensity ($\sim 21\text{-}22 \text{ cm}^{-1}$ max), with smoother curves and less sharp features. Indicates that the material is returning toward its intrinsic, nearly isotropic optical behavior in the plane. The absorption onset shifts marginally higher in energy, consistent with slight band gap widening due to reduced strain. For the 1% strain relative inferences can be possibly drawn, as for the XX and XY absorption spectra almost perfectly overlap, indicating negligible optical anisotropy. Absorption intensity would likely remain around $20\text{-}21 \text{ cm}^{-1}$, slightly lower than the 2% case. Peak structure would smooth out further, with minor shifts in peak positions due to reduced lattice distortion. The absorption onset energy might shift slightly higher, suggesting continued widening of the band gap, consistent with relaxation of the crystal symmetry.

4. Conclusion

This study presents a comprehensive theoretical analysis of the electronic and optical properties of the Janus monolayer WSeTe under varying uniaxial pressure, employing density functional theory (DFT). The findings reveal that WSeTe retains its semiconducting nature throughout the applied pressure range, with a consistent reduction in bandgap. This bandgap narrowing under compression enhances the optical absorption, particularly in the violet region, indicating a promising response for photovoltaic and optoelectronic applications.

The optical conductivity and absorption coefficients show significant enhancement under strain, suggesting WSeTe's viability in next-generation solar cells and nanoscale optoelectronic devices. The material's inherent asymmetry, strong spin-orbit coupling, and polarization properties add to its potential for multifunctional applications, including photodetectors and electromechanical systems.

Thus, WSeTe monolayer, with its tunable band structure and enhanced optical responses under strain, emerges as a promising candidate for future nanoelectronic and optoelectronic devices, supporting ongoing research into 2D Janus materials for advanced technological applications.

5. References

- https://pubs.acs.org/doi/epdf/10.1021/ed5004788?ref=article_penPDF